Effect of alloying on the oxidation behaviour of Co-Al-W superalloys

H-Y. Yan, V. A. Vorontsov, D. Dye*

Department of Materials, Royal School of Mines, Imperial College, Prince Consort Road, London SW7 2BP, UK.

Abstract

The 800 °C isothermal and cyclic oxidation of alloys based on Co-7Al-7W (at.%) was examined. Cr, Fe and Si additions were beneficial. Repeated oxide bilayers formed during cycling of non-Cr alloys, which were not protective ($> 100\,\mu m$ thick). In these layers, the outer was Co_3O_4 and the inner, a porous Co_3O_4 and Al_2O_3 mixture. 10 at. % Cr substitution for Co was sufficient to produce a protective, $\sim 1\,\mu m$ thick scale which contained an outer layer of Al_2CoO_4, a very thin (100nm) middle layer of Cr_2O_3 and an inner layer of Al_2O_3. Therefore protective oxide scales are possible in γ / γ', Co-Co_3(Al,W) superalloys.

Keywords: Oxidation, superalloys, STEM, thermal cycling

1. Introduction

Conventional Co base superalloys are used in high temperature applications due to their combination of good mechanical properties (fatigue, creep and strength), oxidation and corrosion resistance, as well as phase stability at high temperature [1]. The precipitation of carbide phases in Co superalloys contributes significantly to their strength by inhibiting grain boundary sliding. However, large blocky oxidised carbides act as stress concentrators and can initiate fatigue cracks, impairing the mechanical properties at high temperature.

In contrast in the Ni system, the presence of the $L1_2$ Ni_3Al γ' phase, which shows the flow stress anomaly [2], allows precipitation strengthening to provide superior high temperature strength [1]. Therefore, Ni superalloys have come to dominate modern gas turbines, and solid solution Co base superalloys are often restricted to static applications such as vanes and combustors, where their superior environmental resistance and weldability are advantageous [3].

Gas turbine development is driven by the need to increase gas stream temperatures and thereby increase efficiency to decrease fuel burn and CO_2 emissions, particularly at current oil prices [4]. However, the ability to improve Ni superalloy temperature capability by increasing the γ' fraction, solvus temperature or by adding refractory elements is now limited, with the alloy system increasingly being viewed as mature.

Recently, Sato et al. [5] discovered that the Co-Al-W ternary system contains an $L1_2$ γ' phase. This γ' phase has been identified as Co_3(Al,W). With the addition of Ta, the solvus temperature increases substantially, and can be at least $\sim 60\,°C$ greater than the γ' solvus in, *e.g.* Waspaloy. Furthermore, adding Ta dramatically improves the strength [6].

Therefore, Co-Al-W base superalloys are now being considered for use in high temperature applications, and so there is a requirement to understand the oxidation resistance and how it might be tailored through alloying. A few studies have been carried out to examine the oxidation behaviour of this new alloy system [7–11]. A multi-layered oxide structure has been observed in Co-Al-W alloys subjected to exposure in air at 800 °C. It has been found that Co oxides are not protective and suffer from spallation during cooling [11, 12]. Understanding of alloying effects is still limited. In general, it is known that alloying with Cr and Si helps form highly protective oxides of chromia and silica and thus improve the oxidation resistance [13].

It should be noted that gas turbine blades are usually coated with thermal barrier coatings and diffusion barrier layers that also have the effect of reducing the requirement for bare metal oxidation resistance. However, the internal cooling passages of blades are still subjected to elevated temperature, and more importantly so are gas turbine discs. For these requirements current steady-state temperatures in operation are in the region of 650–750 °C, with 800 °C representing an aspiration. Therefore in the present study we focus on the 800 °C condition, in a fine grained wrought-processed polycrystalline material similar to that used in current forged discs.

Rotating polycrystal Ni disc alloys, such as LSHR or ME3, establish a target mass gain for this regime of around $0.2\,mg\,cm^{-2}$ in 200 h at 800 °C. These alloys have Cr contents in the region of 12-16 wt.% and Al contents of around 2-4 wt.%. In comparison, solid solution Co-base alloys in-

*Corresponding author. This version is a regenerated version of the accepted author manuscript that was submitted on 1-Feb-2014.

Email address: david.dye@imperial.ac.uk, T: +44 207 594-6811 (D. Dye)

tended for static applications such as HA-188, with Cr contents of > 20 wt.%, have much better oxidation resistance, but cannot sustain γ' and so are used in static applications. Blade alloys, such as Rene'N5, are primarily alumina formers intended for use above the temperature at which chromia scales become volatile. For comparison, the best Co-Al-W γ/γ' superalloy oxidation performance reported so far gained $3\,\mathrm{mg\,cm^{-2}}$ in this condition [12].

In our previous study [14] we observed that the oxide scales exhibit a three-layered structure. The base metal underneath became depleted of γ', forming a region with a γ matrix and high aspect ratio Co_3W precipitates. Additions of V, Mo, Ti and Ni reduced the oxidation resistance, whereas alloying with Ta, Si, Fe and Cr was beneficial. However, excessive additions of Cr destabilised the γ/γ' microstructure. Ni additions to the Co-Al-W-Cr quaternary were found to stabilise the γ/γ' microstructure whilst retaining oxidation resistance, providing an alloy development strategy to address this shortcoming.

Here we present an in-depth study of the effect of alloying on the oxidation behaviour of Co-Al-W base superalloys at 800 °C, based on variations from a Co-7Al-7W (at. %) alloy. Both isothermal and cyclic oxidation experiments are compared. We then focus on the difference in oxidation sequence and mechanisms between a Co-7Al-7W (at. %) model ternary and its quaternary derivative, Co-7Al-7W-10Cr, where 10 at. % Cr was substituted for Co. It is hoped that the findings will be of utility to the community that is attempting to develop oxidation-resistant Co superalloy successors to Ni superalloys.

2. Experimental procedures

50 g polycrystalline ingots of the alloys studied were prepared by vacuum arc melting under a back-filled argon atmosphere. Each ingot was solution heat treated in a vacuum furnace at 1300 °C for 24 h to eliminate any secondary phases. The ingot was welded into a rectilinear mild steel can packed with Ti powder and super-solvus hot rolled at 1150 °C to obtain $\sim$ 3 mm strip. Each alloy was sealed in quartz tubes back-filled with argon and aged at a temperature 80–100 °C below the γ' solvus. Table 1 lists the nominal compositions of the alloys examined in this study, and each alloy has been given an abbreviated label denoting the nominal atomic fractions of the quaternary and quinary alloying elements. The actual compositions, as measured using inductively coupled plasma optical emission spectroscopy, are listed in our previous work [14].

Isothermal oxidation experiments were then carried out. Cylindrical specimens 3.5 mm in diameter and 2.5 mm thick were wire Electrical Discharge Machined (EDM) from the strip. Specimens were surface ground, cleaned and weighed prior to loading into a Netzsch Jupiter simultaneous Differential Scanning Calorimeter (DSC) / Thermogravimetric Analyser (TGA). A heating rate from room temperature to 800 °C of $10\,^{\circ}\mathrm{C\,min^{-1}}$ was used. During the experiment, dry air was supplied and the total exposure time was 1200 min.

Cyclic oxidation tests were also performed on all ten alloys. $2.5\times2.5\times2.5$ mm cubes were machined from the aged strip using a precision circular saw, the surfaces ground to a surface finish of 0.25µm, cleaned and degreased. Specimens were placed in flat-bottomed alumina crucibles and tested in air at 800 °C in a laboratory furnace. To contain spallation products, lids were placed on the crucibles before weighing during periodic specimen removal and air cooling. Each oxidation cycle was performed according to the following procedure: 1. Placement of the specimens into the furnace at 800 °C. 2. Specimen oxidation in the furnace environment for the allocated period of time. 3. Removal of the specimens from the furnace at 800 °C. 4. Cooling of the specimens from 800 °C to room temperature for approximately 30 mins. 5. Weighing of the specimens using a balance with a resolution of ±0.15 mg. The mass change was measured after 4, 16, 36, 64, 100, 144 and 196 h of exposure.

The morphology, thickness and structure of the oxide layers were examined in a LEO - Field Emission Gun Scanning Electron Microscope (FEGSEM) using samples cold-mounted in acrylic resin, ground, polished and sputter coated with gold. Composition measurements were performed using Energy Dispersive X-ray Spectroscopy (EDS).

Small-volume sections of the oxide layers from the base alloy (Co-7Al-7W) and the 10Cr alloy (Co-7Al-7W-10Cr) were obtained using a Helios NanoLab-DualBeam Focused Ion Beam (FIB). Large grained FIB specimens (Figure 5b) were examined using a JEOL 2000FX Transmission Electron Microscope (TEM) to observe selected area diffraction patterns. An FEI TITAN 80/300 TEM/STEM fitted with a monochromator and an image aberration corrector was used to obtain high resolution lattice images for small grained FIB specimens (Figures 5c,d). "Diffraction patterns" (frequency domain images) were obtained using Fast Fourier Transforms (FFT) in the ImageJ software package. Point EDS analysis was carried out to determine chemical composition in all of the FIB specimens. A JEOL JEM-2100F field emission TEM/STEM with an Oxford Instruments X-Max 80 $\mathrm{mm^2}$ silicon drift EDS detector was used to obtain chemical composition maps of selected FIB specimens. A low background beryllium double-tilt holder was used to support the foils.

3. Results

Mass change data for the isothermal oxidation tests are shown in Figure 1. It should be noted that the instrument reports incremental changes, whereas the total mass change is reported here. The fluctuation in the mass change data shortly after 300 min are an experimental artefact associated with the building services management of the laboratory air handling system.

Figure 1a displays (i) approximately parabolic growth behaviour, (ii) continuous mass gains because the spallation products were retained, and (iii) a ranking of the alloys from best to worst as follows: 10Cr > 20Fe > 1Si > 20Ni > 2Ta > Base > 2Mo > 2Ti > 6Ni-4V > 2V.

Oxide film growth is expected to be parabolic with time [15] if oxidation is diffusion controlled, if there is no change in mechanism and only up to the point where cracking and/or spallation occurs. Very commonly such conditions are not obeyed. Nevertheless, it is common in the literature to calculate parabolic rate constants (K_p) from the gradient of figures such as Figure 1b, assuming behaviour according to (mass change)$^2 = K_\mathrm{p}t$, where mass change is measured in mg cm^{-2}, time (t) is in hours and K_p, is in mg^2 cm^{-4} h^{-1}. The Wavemetrics Igor Pro software package was used to obtain the parabolic rate constants provided in Table 1.

In the present case, in both the isothermal and cyclic tests, spallation and cracking occurred during exposure. However, spalled oxides were contained in the sample crucible and so the data accommodates the effects of spallation even though the rate constants do not reflect a simple diffusion-controlled situation. The plots in Figure 1b are close to fitting the classic view of high temperature oxidation, and therefore these rate constants are regarded as being of engineering utility.

Figure 2 shows a back scattered electron image of the base alloy after 20 h of isothermal oxidation at 800 °C. The thickness of the oxide has been measured (using ImageJ) and the average thickness was 36 μm. The image shows that there are two distinct oxide layers. The outer layer is porous. Point EDS analysis has shown that the outer layer is a Co rich oxide and the inner oxide layer contains Co, Al and W. The outermost metal substrate has precipitated the undesirable intermetallic phase Co_3W and is also denuded of γ'.

During cyclic oxidation experiments oxides spall non-uniformly during cooling. This can lead to the weight of the specimen decreasing with increasing cycle number [16]. In our study, the total mass of the oxidised specimens increases with increasing exposure time, Table 2. This is because most of the spallation products were contained inside the crucibles. In the case of the 10Cr and 1Si alloys after 144 hours exposure in the furnace, the weight of the samples was found to decrease. This was because the crucibles were not covered during the exposure to ensure a free supply of air. Once the furnace door was opened, the inflow of cooler room temperature air caused the fur-

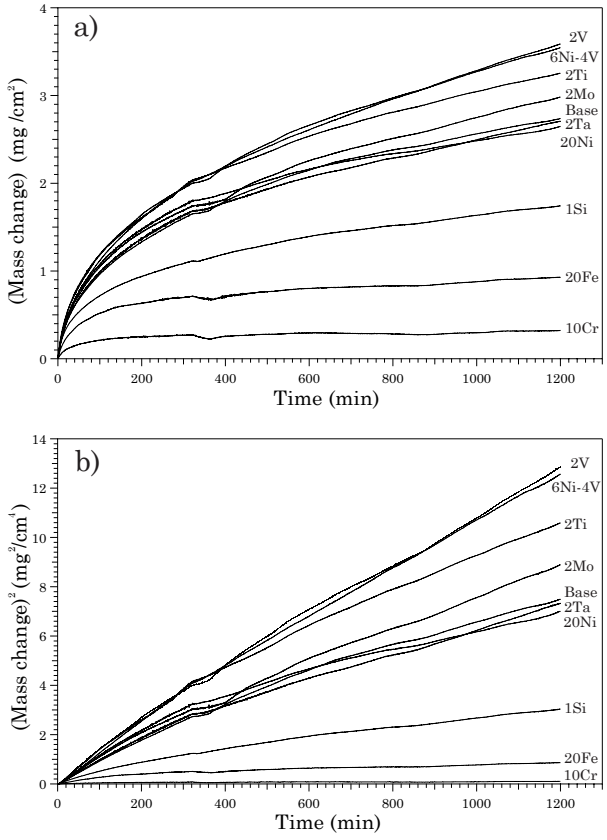

Figure 1: Mass change data from the isothermal oxidation experiment at 800 °C for 20 h, (a) plotted as mass change vs. time and (b) as (mass change)^2 vs. time. The alloy designations are provided in Table 1.

Table 1: Rate constants (mg^2 cm^{-4} h^{-1}) for the isothermal oxidation experiments performed at 800 °C for 20 h.

Alloy (at. %)	**Label**	**Rate constants**
76Co-7Al-7W-10Cr	10Cr	0.003
66Co-7Al-7W-20Fe	20Fe	0.032
85Co-7Al-7W-1Si	1Si	0.139
66Co-7Al-7W-20Ni	20Ni	0.315
86Co-7Al-5W-2Ta	2Ta	0.339
86Co-7Al-7W	Base	0.365
86Co-7Al-5W-2Mo	2Mo	0.426
86Co-6Al-6W-2Ti	2Ti	0.507
80Co-7Al-3W-6Ni-4V	6Ni-4V	0.616
86Co-7Al-5W-2V	2V	1.161

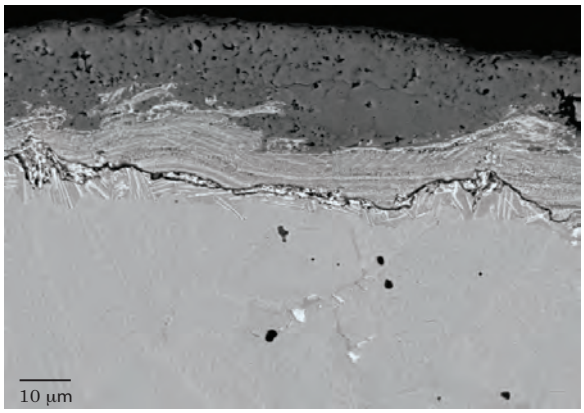

Figure 2: Back scattered electron image of the oxide scale formed on the base alloy after 220 h isothermal oxidation at 800 °C.

Table 2: Mass change data ($mg\,cm^{-2}$) for Co-Al-W base alloys subjected to cyclic oxidation at 800 °C, from our previous study [14].

Alloy	**Time (h)**							
	0	4	16	36	64	100	144	196
10Cr	0	0	0	0.6	0.9	2.0	0.9	0.9
20Fe	0	1.2	1.2	1.5	2.3	2.5	2.5	2.5
1Si	0	0.7	2.2	4.7	5.0	7.9	6.8	7.6
2Ta	0	1.8	4.0	5.8	7.1	7.4	7.9	8.2
Base	0	2.2	4.0	7.4	7.7	9.5	9.8	12.9
20Ni	0	3.2	5.3	7.7	8.4	11.6	12.7	14.1
2Ti	0	2.1	4.8	6.6	7.5	9.9	10.5	14.4
2Mo	0	2.0	4.9	6.4	9.8	12.8	14.7	18.9
2V	0	2.0	4.3	7.5	10.7	14.7	17.3	22.2
6Ni-4V	0	2.3	4.1	7.6	10.8	14.6	18.8	23.1

nace temperature to drop temporarily by an amount that is difficult to quantify. This temperature drop resulted in some minor oxide spallation prior to the lids being placed over each crucible.

Both the isothermal and cyclic oxidation experiments show that the addition of Cr, Fe and Si to the Co-Al-W base alloys improved the oxidation resistance. Alloying Mo and V into the alloys had a negative effect on the oxidation behaviour. Both of these oxides are have poor adherence to the substrate and are volatile at temperatures as low as 600 °C, which can lead to catastrophic oxidation that can result in component cracking [17]. Vanadium oxide is also undesirable for its 'pest' effect, whereby it can contaminate other non V containing components of the turbine and adversely affect their oxidation performance [32]. The order of decreasing oxidation resistance of the alloys from the cyclic tests is 10Cr > 20Fe > 1Si > 2Ta > Base > 20Ni > 2Ti > 2Mo > 2V > 6Ni-4V.

The back scattered electron images shown in Figure 3 were taken from cross sections of the specimens after 196 hours cyclic oxidation at 800 °C. Multilayer oxide scales can be seen in the base, 2Mo, 2V and 6Ni-4V alloys. The overall oxide thicknesses in these alloys were in excess of 100 μm (Table 3). It can be noted that in the micrograph of the 2V alloy in Figure 3 the outermost layers appear brighter. However, EDS mapping showed that this was an artefact arising from localised charging in the specimen during imaging and did not correspond to an increased concentration of elements with greater atomic mass. From the contrast in the back scattered electron images, three different regions can be observed in the oxide scales of the 2Ti, 2Ta, 20Ni, 20Fe and 1Si alloys. Voids were also found in the 2Ti, 2Ta, 20Ni and 1Si alloys at the oxide/metal interface. Their form was suggestive of a vacancy formation mechanism. The voids weaken the adherence of the oxide layers and promote spallation. The voids in the 20Fe alloy are smaller and fewer in number. This is one way to rationalise the finding that the 20 at. % Fe addition improved the oxidation resistance. The alloy containing 10 at.% Cr

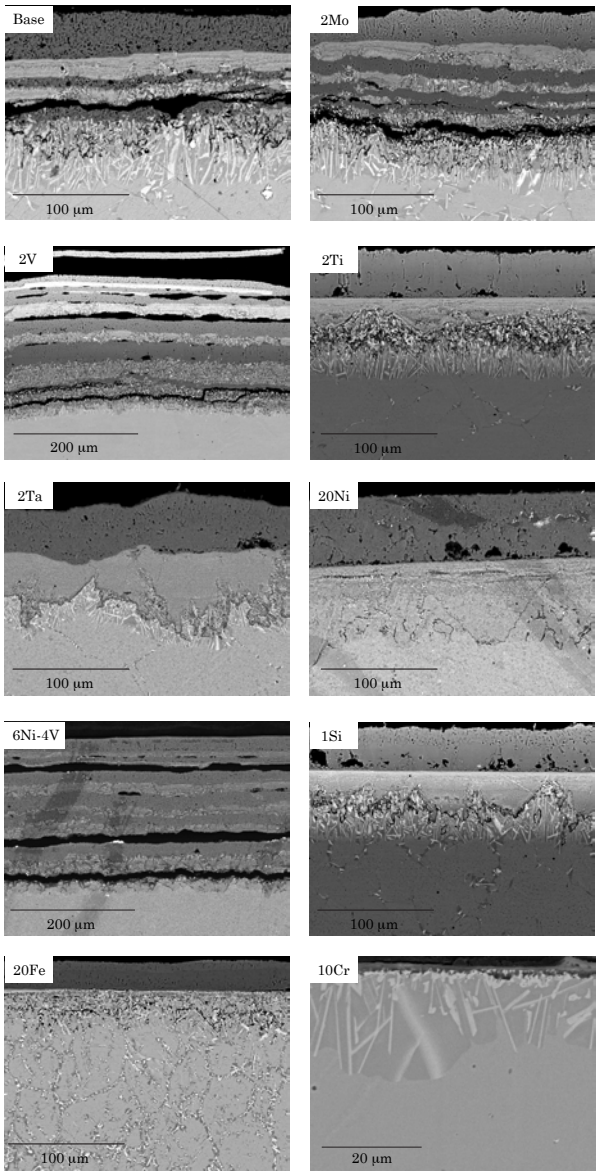

Figure 3: Back scattered electron images of the oxide scales formed in all the alloys examined after 196 h cyclic oxidation in air at 800 °C. N.B. different scale bars for the V- and Cr- containing alloys.

to formed the thinnest oxide scale ($\sim 1.3\,\mu$m). This thin layer of oxide appears to have been truly protective, limiting further oxidation. In all of the oxidised specimens, similar to the isothermal oxidation specimens, needle shaped intermetallic precipitates of Co_3W were found in the outermost layer of the metal substrate.

To identify the different oxide layers, EDS mapping was carried out on all the specimens. Due to overall similarities between the specimens, only the base and 10Cr alloys will be discussed here. Figure 4 shows an EDS map of the base alloy. It can be seen that alternating oxide layers with different chemical compositions formed. The outer layer is mainly composed of Co containing oxide, with some Al. Underneath this, a layer enriched in Al and W is found. It is known that the interaction volume of the electron beam

Table 3: Comparison of the mean oxide thicknesses observed after 196 h cyclic oxidation at 800 °C.

Alloy	Oxide thickness μm
Base	106±12
2Mo	115±15
2V	158±24
2Ti	83±4
2Ta	54±9
20Ni	119±7
6Ni-4V	168±11
1Si	78±5
20Fe	50±7
10Cr	1.3±0.4

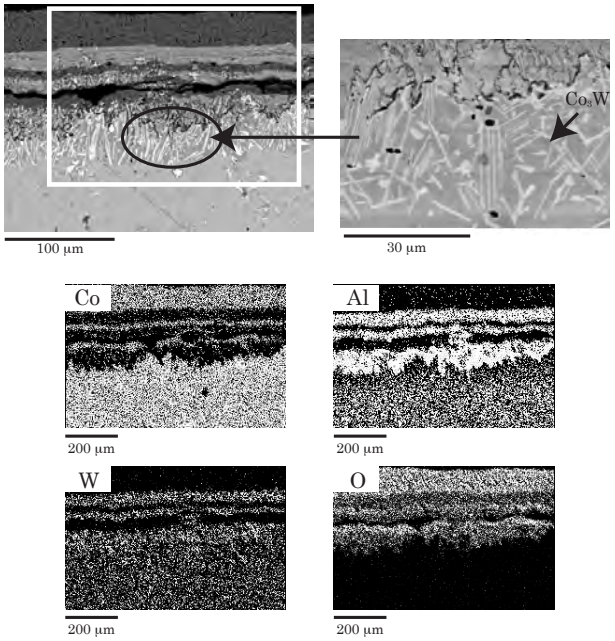

Figure 4: Backscatter electron image (top) for the base Co-7Al-7W alloy after 196 h cyclic oxidation at 800 °C, and corresponding elemental SEM-EDS maps (bottom).

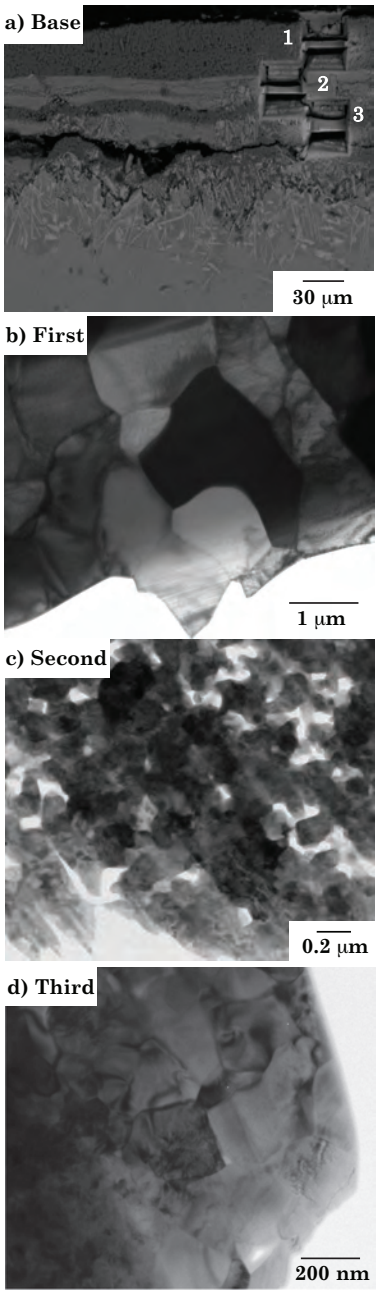

Figure 5: Backscatter electron image from the base alloy subjected to 196 h cyclic oxidation at 800 °C after sectioning by FIB milling (a) and bright field TEM images from each layer (b-d).

can up to 6 μm deep [18] and the accuracy of chemical composition determination in EDS analysis is $\sim 2\%$ [19].

Co can form one of three possible oxides at high temperatures. CoO has cubic rock salt structure with a lattice constant of 4.26 Å[20]. It is stable above 900 °C [21]. Co_3O_4 is another stable oxide that has a cubic spinel structure with a lattice constant of 8.15 Å[22]. Under readily attainable oxygen partial pressures, it is thermodynamically favourable to form Co_3O_4 [23]. The third type of oxide is Co_2O_3, which is thermally unstable, typically being obtained electrochemically under carefully controlled conditions [24, 25].

Due to the accuracy limitations of EDS analysis, it can be difficult to distinguish between CoO, Co_2O_3 and Co_3O_4. Therefore, to determine the type of oxide that forms in these layers, small-volume sections of the oxide layers were obtained from FIB, and selected area electron diffraction patterns were obtained from individual grains in the TEM. The lattice constants were calculated from each diffraction pattern, the calculated lattice constants were compared to the literature values and thus the type of Co oxide determined. Figure 5a shows the back scattered electron image of the base alloy after sectioning and lift out in the FIB. The first three layers from the oxide specimen were investigated.

Bright field TEM images for the first three oxide layers

from the base alloy are shown in Figure 5b-d. The average grain size in the first layer is $\sim$ 2-3 μm. Six grains were examined using convergent beam TEM EDS and the average chemical composition calculated. The average chemical compositions for each layer are listed in Table 4. The average chemical composition for the first layer was 43 Co – 57 O (at. %), which suggests that the oxide would be Co_3O_4. However, given that the oxygen contents for the three oxides are quite similar – 50 at.% for CoO, 57 at. % for Co_3O_4 and 60 at. % for Co_2O_3, it is prudent to also make use of the structural information available from the electron diffraction patterns. An example of a selected area diffraction pattern is shown in Figure 6a. The zone axis has been labelled in the pattern, and the diffraction pattern was compared to the simulated diffraction pattern generated using the Crystal Maker software using a crystal structure from the literature [22]. The average lattice constant for the first layer was measured to be 8.20 Å. This value is close to the lattice constant in Co_3O_4 – 8.15 Å [22] This confirms that the first layer oxide from the base alloy is Co_3O_4. Chemically, only Co and O were detected in the TEM. No Al can be quantified in these grains, but EDS mapping in the SEM (Figure 4) showed trace amounts of Al. This discrepancy is either due to the differences in the volume of material sampled by the electron probes in the two instruments, or the fact that some sparse localised grains of Al containing oxide exist in the bulk oxide that were not present in the FIB section used for TEM.

The second oxide layer is porous. The average chemical composition for the middle layer is 25 Co – 10 Al – 3 W – 62 O (at.%). This suggests that mixed oxides could be formed in this layer. The average grain size in this layer is much smaller than in the first layer and most of the grains in the TEM specimen overlap. The grain size is less than 200 nm, which is beyond the limit of conventional diffraction analysis in the JEOL 2000FX TEM. Therefore, it was impossible to obtain selected area diffraction patterns from this layer. For this reason, the high-resolution phase contrast imaging of the lattice was performed on 6 grains using the FEI TITAN 80/300 TEM. Examples of frequency domain images are shown in Figure 6b-c. Measuring the angles and distances between the spots in the frequency domain images and comparing them to the simulated diffraction patterns suggests the presence of two oxides: Co_3O_4 and Al_2O_3. The average lattice constant of Co_3O_4 in the second layer was measured to be 8.14 Å. Al_2O_3 has a trigonal structure with average lattice constants of a = 4.77 Å and c = 13.0 Å. These measured lattice parameters matched closely the literature values a = 4.76 Å and c = 13.0 Å [26].

Table 4: Average chemical compositions (at.%) for each oxide layer examined in the base Co-7Al-7W alloy after 196 h cyclic oxidation at 800 °C.

Layer	Co	Al	W	O	Oxide
First	43 ± 4	–	–	57 ± 3	Co_3O_4
Second	25 ± 2	10 ± 2	3 ± 2	62 ± 2	Co_3O_4/Al_2O_3
Third	37 ± 4	–	–	63 ± 4	Co_3O_4

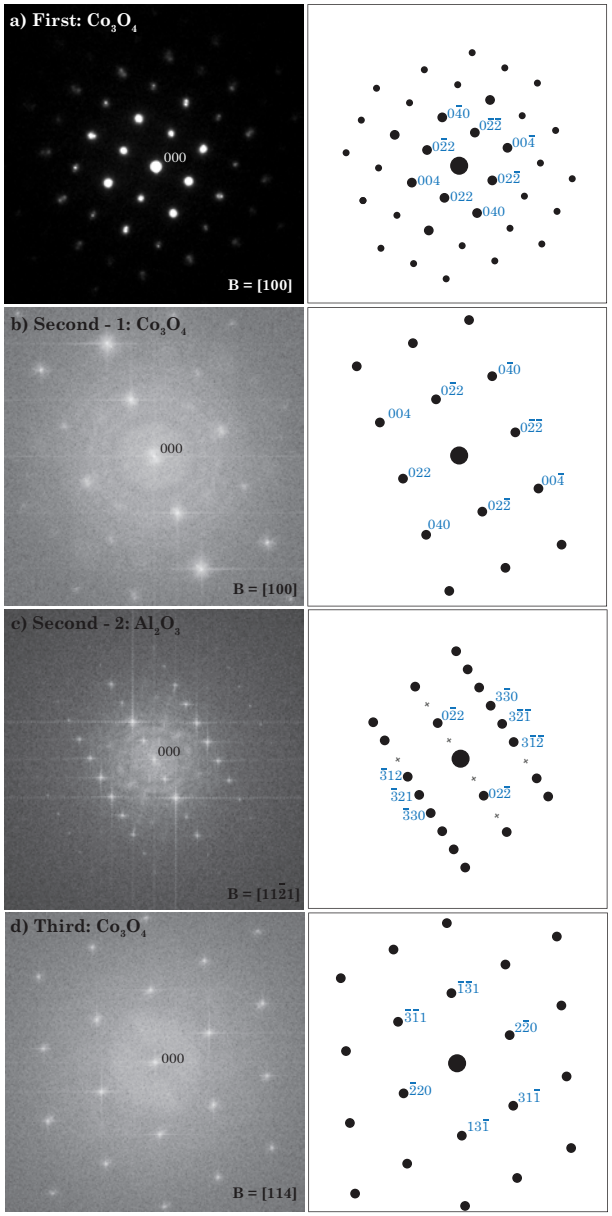

Figure 6: Selected area diffraction pattern from the first layer (a) and frequency domain images from the second (b-c) and (d) third layers (left), formed in the base alloy after 196 h cyclic oxidation at 800 °C, and corresponding simulated diffraction patterns (right).

In order to confirm this conclusion chemically, EDX mapping was performed using a JEOL JEM-2100F microscope fitted with a solid state EDX detector, Figure 7. The combination of probe current and detector sensitivity in this TEM meant that elemental mapping was possible. This showed that two distinct groups of compositions could be observed. The first group contained Al and Co in similar quantities, which confirmed that Co_3O_4 and Al_2O_4

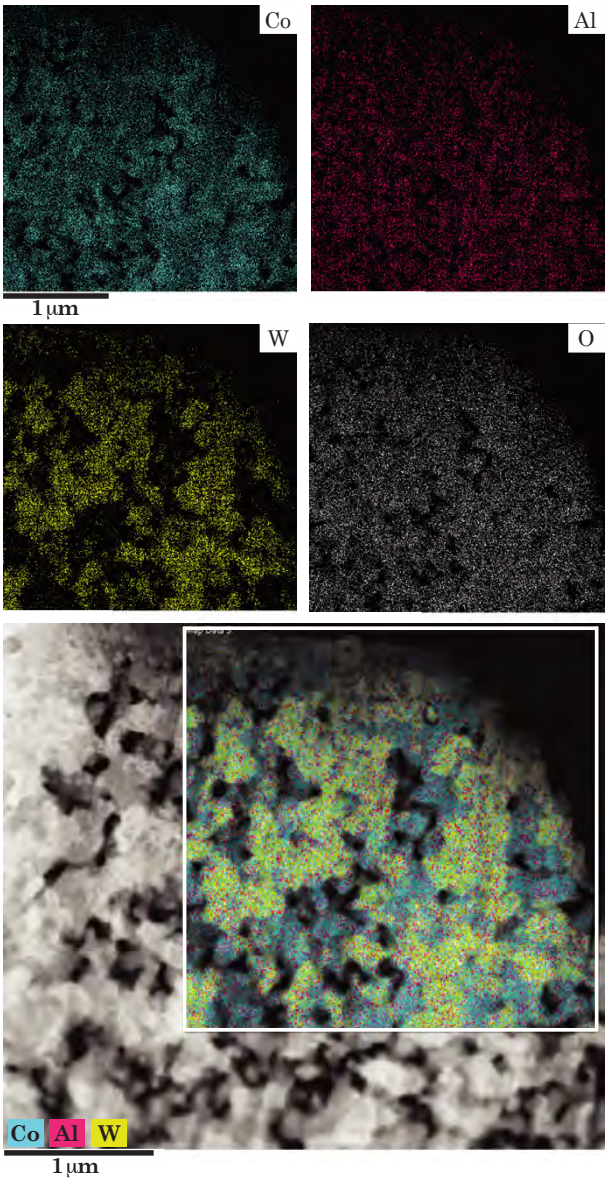

Figure 7: STEM-EDS map obtained from the second oxide layer of the base alloy subjected to cyclic oxidation at 800 °C for 196 h.

co-exist in the middle layer. The grains of the two types of oxide overlapped and could not be distinguished from one another in the mapping. The solubility for Co on the Al site is limited in alumina in this case. However, it is worth noting that some solubility of Co in Al_2O_3 is possible, but this only occurs at very high temperature $\sim$ 1300 °C [27]. The second group contained significant quantities of W, implying that there is some solubility for W in the Co_3O_4 phase.

The average chemical composition of the third layer was found to be 37 Co – 63 O (at. %); the oxygen content in the third layer was higher than that in the first. At the triple junctions the average chemical composition was found to be 30 Co – 3 Al – 67 O (at. %). An example of the frequency domain image is shown in Figure 6d. The average grain size was $\sim$ 200 nm, therefore high resolution TEM was also used to determine the oxide phase. The average lattice constant of the tested grains was 8.12 Å, confirming that the third layer oxide is also Co_3O_4. EDS has also shown that that the triple junctions were enriched in Al. As was the case with the first layer, TEM imaging showed that there were no alumina grains present in the regions examined.

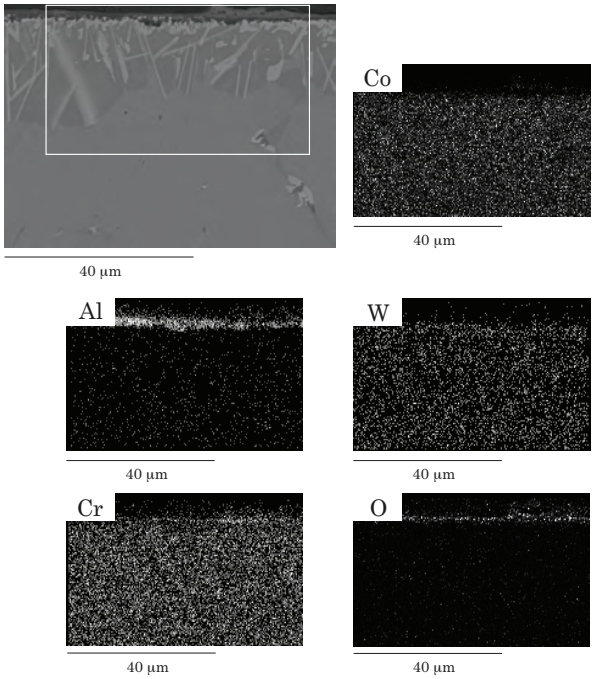

Figure 8: Backscatter electron image of the oxide scale formed in the 10Cr alloy subjected to cyclic oxidation at 800 °C for 196 h, and EDS maps of the elements present, obtained in the SEM.

The oxide scale grown in the 10Cr alloy is shown in Figure 8. A very thin oxide scale ($\sim$ 1.3 μm) was formed on the alloy surface, and the EDS results show that this scale is Al rich. Examining the scale at higher magnification using STEM imaging and STEM-EDS mapping reveals structure of the oxide scale in finer detail, Figures 9 and 10.

To determine the crystal structure and the actual composition of this thin oxide scale, small-volume sections of the 10Cr oxide were obtained by FIB milling and exam-

Table 5: Chemical compositions (at.%) obtained by point TEM-EDS (FEI Titan) for grains in the distinct surface layers formed in the 10Cr alloy after 196 h cyclic oxidation at 800 °C. * small traces < 0.3 at. %. The Co_3W analysis was performed in order to confirm the composition of the DO_{19} high aspect ratio phase in the base metal.

Layer	**Co**	**Al**	**Cr**	**W**	**O**	**Oxide**
Outer	11 ± 1	25 ± 2	1 ± 1	–	63 ± 2	Al_2CoO_4
Middle	6 ± 5	5 ± 3	22 ± 7	1 ± 1	66 ± 2	CrO_2/Cr_2O_3
Inner	*	36 ± 4	1 ± 2	*	62 ± 3	Al_2O_3
Co_3W	78 ± 2	1 ± 1	6 ± 3	12 ± 3	3 ± 3	

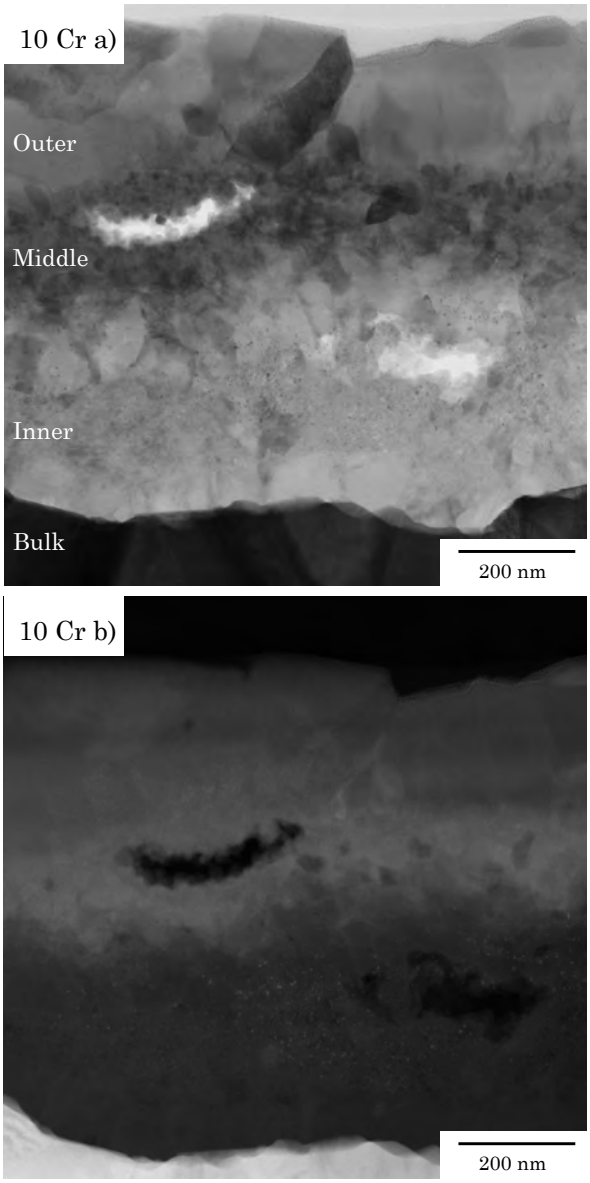

Figure 9: Overview of the oxidised surface in the 10Cr alloy after 196 h of cyclic oxidation at 800 °C obtained from a FIB-milled TEM foil using (a) bright field and (b) HAADF STEM imaging modes.

ined in the TEM. Figure 9a is a bright field STEM image of the 10Cr oxide which shows strong diffraction contrast, enabling the grain size of the oxides to be determined. In contrast, Figure 9b is the High Angle Annular Dark Field (HAADF) image. The contrast depends strongly on the atomic number, Z, of the atoms in the specimen. Regions containing higher concentrations of heavier elements scatter more electrons at high angles and therefore appear brighter. The Z-contrast in the image shows clearly that the scale in the 10Cr alloy consists of three different layers after high temperature cyclic oxidation.

Larger grains $\sim$ 100-200 nm in size were observed in the outer layer (by using ImageJ to estimate sizes from Figure 9). The compositions of six grains in the outermost

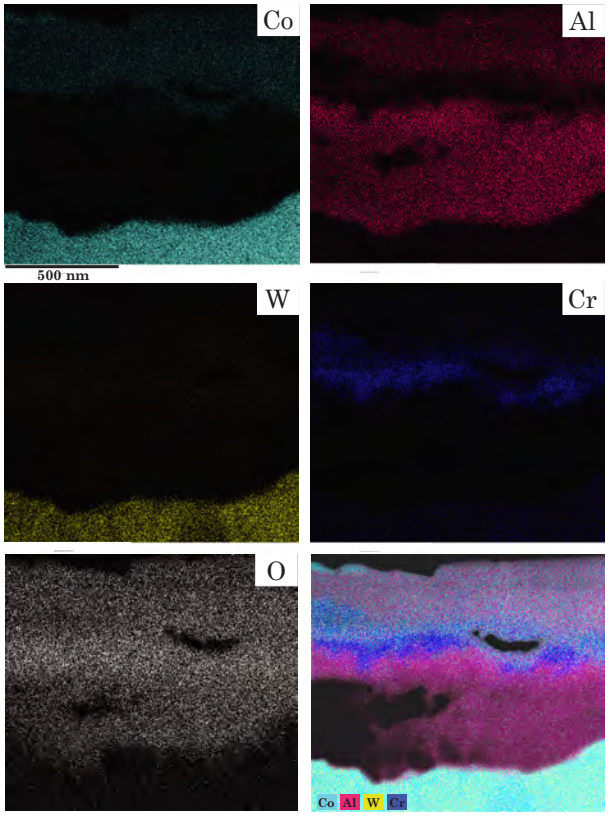

Figure 10: STEM-EDS map of the oxidised surface obtained for the 10Cr alloy after 196 h cyclic oxidation at 800 °C.

layer were determined by point EDS, and the average is provided in Table 5. This oxide contained Al, Co, O and small traces of Cr, with an average chemical composition of 25 Al – 11 Co – 63 O – 1 Cr (at. %). To confirm the oxide phase, high-resolution phase contrast lattice imaging was performed. The frequency domain image (Figure 11a) was compared to a simulated diffraction pattern of Al_2CoO_4 (cobalt blue). Al_2CoO_4 has a cubic spinel structure with lattice constant of 8.11 Å [28]. The average lattice constant for the tested grained is 8.10 Å, which it is close to the literature value. These observations confirm that the outer layer of the 10Cr alloy is Al_2CoO_4. The alumina Al_2O_3 structure could not be matched to any of the frequency domain images for the outer layer and can therefore be excluded.

The middle layer consisted of fine oxide grains. The average size of these was in the range of 30 to 40 nm. Point EDS showed that the average chemical composition for this layer was 22 Cr – 66 O – 6 Co – 5 Al – 1 W (at. %), which confirms that the middle layer is Cr rich. Two types of Cr oxides were found in the frequency domain images. Figure 11b shows a frequency domain image matched by a simulated diffraction pattern for CrO_2, which has a tetragonal structure. The lattice constants are a, b = 4.42 Å, c = 2.92 Å[29]. The measured average lattice constants for this oxide were, b = 4.42 Å, c = 2.91 Å, which closely match the literature values. Cr_2O_3 was also found in the middle

layer (Figure 11c). It has a trigonal structure with lattice constants of a = 4.96 Å, c = 13.60 Å[30]. The measured average lattice constants were a = 4.87 Å, c = 13.56 Å. Only CrO_2 and Cr_2O_3 were found in the frequency domain images, but small traces of Co, Al and W were detected by point EDS. This suggests that there is some solubility of Co, Al and W in these oxides. It may also explain why the measured lattice constants in the Cr_2O_3 were slightly different from literature values.

The grain size in the inner layer oxide varied between 50 and 200 nm. The average chemical composition of this layer was 36 Al – 62 O (at. %). This was confirmed to be Al_2O_3 with an average calculated lattice constant of a = 4.77 Å. The preferred crystal orientation for this oxide is B = [0001], therefore it is not possible to obtain c lattice parameter. In this layer, small bright spots/clusters were observed within this inner oxide layer in Figure 9b. On average, these were found to be 5–10 nm in size. By using a STEM EDS line profile, it was found that heavier elements (mostly Cr and to a lesser extent Co and W) were present in these spots.

One should note that spots which are systematic absences in the simulated diffraction patterns, denoted by the asterisk symbol (∗), are present in the corresponding electron diffraction pattern, Figures 6(c), and frequency domain images, Figures 11(a) and (b). Possible reasons for this could be the non-stoichiometric nature of the oxides and (in the case of HR TEM) the inability to image or resolve all of the atomic columns in the crystal lattice.

4. Discussion

In this study we have compared the isothermal and cyclic oxidation behaviour of Co-Al-W base alloys at 800 °C. Both experiments show that alloying Cr, Fe and Si into the Co-Al-W base alloys improved the oxidation resistance and adding that V is very deleterious. The mass changes obtained under cyclic oxidation at 16 hours were greater than under isothermal oxidation at 20 hours. Therefore, oxygen attack on the alloys was more severe during cyclic oxidation. This is because the metal substrates and the oxide scales have different coefficients of thermal expansion and so large stresses are generated during cooling, causing cracking and spallation. Under isothermal conditions parabolic behaviour was obtained. However, the gas turbines are subject to temperature cycling over each flight and thus cyclic oxidation experiments are more representative of these conditions. It has been suggested that during cyclic oxidation, each cycle can result in spallation. On re-heating, freshly uncovered regions then behave like a new metal surface, resulting in accelerated overall oxidation [31]. The oxide spallation that results makes the diffusion of oxygen more difficult to predict and control [16]. In the present case, cyclic oxidation, as well as providing an engineering test more representative of actual gas turbine operation, also provided a very similar ranking to the isothermal tests.

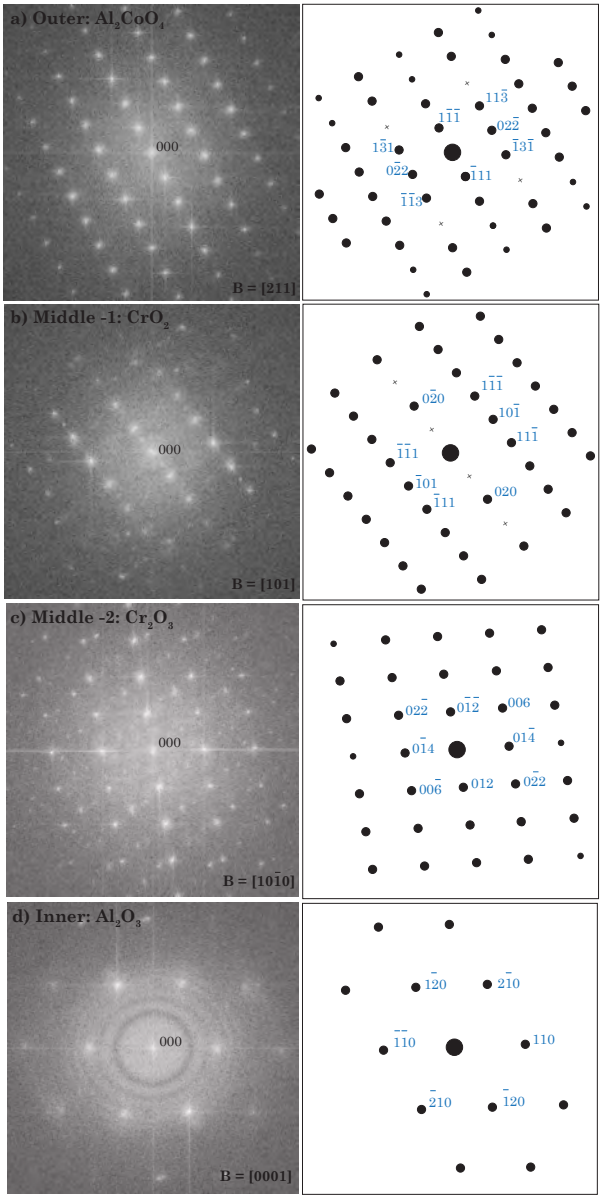

Figure 11: Frequency domain images (left) from the oxide layers in the 10Cr alloy after 196 h cyclic oxidation at 800 °C, and the corresponding simulated diffraction patterns (right).

Our study has also identified a change in the mechanisms of oxide scale formation between the base alloy and the alloy containing 10 at. % Cr. The observations show that two different oxide layers were formed by the base alloy in air at 800 °C. EDS mapping showed that the oxide scales in the base alloy alternated between Al-free and Al containing oxides, with the point EDS and diffraction patterns from TEM demonstrating that the outermost layer was Co_3O_4. Underneath this a complex mixture of porous oxides formed, with high resolution lattice imaging showing that both Co_3O_4 and Al_2O_3 occurred. Below this complex porous oxide, a thinner layer of Co_3O_4 with a smaller grain size was found.

A schematic view of the oxide scale grown on the base

alloy is shown in Figure 12a. The current understanding of the oxide formation mechanisms in Co-Al-W alloys is limited. We propose the following scheme for the scale formation: firstly oxygen diffuses inwards through the alloy. With the high Co content in the alloy, the formation of the stable Co_3O_4 is favoured at 800 °C. The partial pressure of oxygen and depletion of Co from the base metal then favour the formation of Al_2O_3 at the metal/oxide interface, forming the second oxide layer. This then results in the removal of Al from the base metal and consequently the precipitation of Co_3W. The remaining Co also oxidises to form finer grained Co_3O_4. This process produces a continuous and distinct porous layer in the scale, composed of the two phases, which therefore cannot coarsen and so remains very fine grained.

Other alloys not containing Cr form oxide scales with multiple layers, in the same manner as the base alloy, whereby the two types of layers alternate. The top layer is comprised of Co_3O_4 grains, while the underlying layer is a mixture of oxides containing Co_3O_4 and Al_2O_3. In the case of the base, 2Mo, 2V and 6Ni-4V alloys under cyclic oxidation several of these layers appear to have formed in alternation with each pair separated from the next by some voids/cavities. In the 2Ti, 2Ta, 20Ni, 1Si and 20Fe we only observe three layers, with the innermost being similar to the outermost and also consisting of Co_3O_4 grains. These alloys have a smaller parabolic rate constant and given more time, it is possible that further layers would form. Knowledge of oxygen solubility and diffusivity in Co-based ternary and quaternary systems is limited. Addition of relatively inert elements can have a dramatic effect on the oxidation resistance of an alloy [32]. We suggest that the multiple alternating layers form due to cracking associated with each cooling cycle, which then raises the oxygen partial pressure at the metal / oxide interface and allows re-establishment of the Co_3O_4 growth mode. Once a sufficient thickness of this layer formed, then the alumina-containing scale began to form once again, until cracking reoccurred, repeating the cycle.

Figure 12b shows a schematic view of the cross section of the oxidised 10Cr specimen. The most important fact is that with 10 at. % Cr in the alloy, the oxide thickness is significantly thinner (by two orders of magnitude) than the base alloy. Thus one can conclude that the oxidation resistance is improved dramatically. The bright field image (Figure 9a) shows that three layers of oxides formed in this specimen. The outer oxide layer was Al_2CoO_4. This oxide is thermally stable and is usually synthesised at temperatures exceeding 1200 °C by a solid state reaction between CoO and Al_2O_3 [33]. The mechanism of formation of Al_2CoO_4 in the present case is unclear. A possible reason could be that during the early stages of oxidation Co and Al react with oxygen and form Co_3O_4 and Al_2O_3, and then 10 at. % Cr in the alloy promotes a reaction between these phases at 800 °C, which produces the Al_2CoO_4.

CrO_2 is found in the middle layer. Formation of CrO_2 is not yet understood. It is known that under ambient

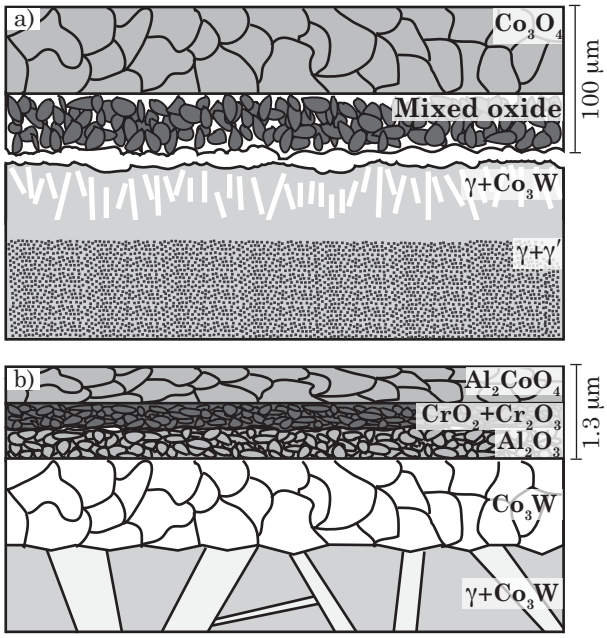

Figure 12: Schematic representation of the oxide scales grown in (a) Co-7Al-7W and (b) Co-10Cr-7Al-7W (at. %) after 196 h of cyclic oxidation at 800 °C.

oxygen partial pressure at temperatures above 300 °C, this oxide becomes thermodynamically unstable. It is usually produced by decomposition of precursor compounds under high oxygen partial pressures under hydrothermal conditions [34]. The middle layer contains another type of oxide - Cr_2O_3. Chromia has low diffusivity and improves oxidation resistance because it is stoichiometric and therefore has very limited diffusivity for O. Although at > 1000 °C it becomes unstable [35], chromia-containing scales are usually found to be more corrosion and sulphidation-resistant than alumina scales are therefore usually felt to be desirable.

With most of the Co consumed in the formation of $AlCo_2O_4$, Al_2O_3 forms in the inner oxide layer by internal oxidation. Al_2O_3 has even lower diffusivity for O than Cr_2O_3, which further slows the migration of reactive species through the oxide scale and protects the alloy. Furthermore, Al_2O_3 has better high temperature stability than Cr_2O_3.

While the base alloy also forms Al_2O_3, the amount formed is not sufficient to form a protective scale. Furthermore, the Al_2O_3 containing layer is porous and contains Co_3O_4. Therefore, the formation of protective scales of Cr_2O_3 and Al_2O_3, as observed in the 10Cr alloy, requires a minimum amount of both Cr and Al. Below these critical levels, fast growing base metal oxides form.

5. Conclusions

This study shows that oxidation-resistant, protective oxide scales can be formed in γ/γ', Co–Co_3(Al,W) superalloys. The following conclusions can also be drawn:

1. Both isothermal and cyclic oxidation experiments at 800 °C show that alloying Cr, Fe and Si into Co-7Al-7W improved oxidation resistance, whereas V was detrimental.

2. Multilayer oxide scales were observed in the base, 2Mo, 2V and 6Ni-4V alloys under cyclic oxidation. Three regions of interest formed in the 2Ti, 2Ta, 20Ni, 1Si and 20Fe alloys. The thickness of these scales were greater than 100 μm.

3. A very thin oxide scale ($\sim 1\,\mu$m) was formed when 10 at. % Cr was substituted for Co in the alloy.

4. The oxide scale in all alloys not containing Cr comprised of two types oxide layers. The outer layer was Co_3O_4 and the inner layer was a porous scale containing both Co_3O_4 and Al_2O_3. W was detected in this layer, but we found no direct evidence for the presence of a tungsten oxide phase. The two layers appear to periodically partially delaminate from the alloy substrate, exposing its surface to air whereby it can grow another pair of layers. This process produced the characteristic multi layer oxide scale, which possesses little benefit to oxidation resistance.

5. It is clear that the addition of Cr changes the mechanism of oxide scale formation. Three layers of oxides were found in the 10Cr alloy under cyclic oxidation. The outer layer was Al_2CoO_4, the middle layer was enriched with Cr and contained both CrO_2 and Cr_2O_3, whilst the inner layer is Al_2O_3. These three layers with low oxygen diffusivity adhere well to the substrate and each other and so protect the alloy against high temperature oxidation.

6. Multiple techniques have been used to investigate the oxidation behaviour of these Co-Al-W based alloys. This study has shown that a critical amount of both Al and Cr is required to form a protective oxide scale. It also highlights the importance of using high-resolution imaging techniques when studying thin oxide scales in multicomponent alloys.

6. Acknowledgements

The authors would like to acknowledge the financial support provided by Rolls-Royce plc and EPSRC (UK) under the Dorothy Hodgkin Postgraduate Awards scheme (H-Y.Y) and by grant EP/H004882/1 (D.D., V.A.V.). Useful conversations with Mark Hardy at Rolls-Royce plc. are also acknowledged. We would also like to thank Richard Sweeney and Ecaterina Ware for their assistance.

7. References

[1] C. T. Sims and W. Hagel. The Superalloys, first ed., John Wiley & Sons, New York, 1972, pp. 287-314.

[2] J. H. Westbrook, Temperature-dependence of the hardness of secondary phases common in turbine bucket alloys, Trans. AIME, 209 (1957) 898–904.

[3] J. R. Davis editor, Nickel, Cobalt and their Alloys, ASM Intl., first ed., Ohio, 2000.

[4] P. C. Ruffles, Aero engines of the future, Aeronaut. J., 107 (2003) 307–321.

[5] J. Sato, T. Omori, K. Oikawa, I. Ohnuma, R. Kainuma, and K. Ishida, Cobalt-base high-temperature alloys, Science, 312 (2006) 90–91.

[6] A. Suzuki, G. C. DeNolf, and T. M. Pollock, Flow stress anomalies in γ/γ' two-phase Co-Al-W-base alloys, Scr. Mater., 56 (2007) 385–388.

[7] Y. T. Xu, T. D. Xia, J. Q. Yan, and W. J. Zhao, Effect of alloying elements on oxidation behavior of Co-Al-W alloys at high temperature, Chin. J. Nonferr. Met., 20 (2010) 2168–2177.

[8] L. Klein, Y. Shen, M. S. Killian, and S. Virtanen, Effect of B and Cr on the high temperature oxidation behaviour of novel γ/γ'-strengthened Co-base superalloys, Corros. Sci., 53 (2011) 2713–2720.

[9] L. Klein and S. Virtanen, Electrochemical characterisation of novel γ/γ'-strengthened Co-base superalloys, Electrochimica Acta, 76 (2012) 275–281.

[10] L. Klein and S. Virtanen, Corrosion properties of novel γ'-strengthened Co-base superalloys, Corros. Sci., 66 (2013) 233–241.

[11] H. Y. Yan, V. A. Vorontsov, J. Coakley, N. G. Jones, H. J. Stone, and D. Dye, Quaternary alloying effects and the prospects for a new generation of Co-base superalloys, in: E. S. Huron, R. C. Reed, M. C. Hardy, M. J. Mills, R. E. Montero, P. D. Portella, J. Telesman (Eds.), Superalloys 2012, John Wiley & Sons, New Jersey, 2012, pp. 705–714.

[12] L. Klein, A. Bauer, S. Neumeier, M. Göken, and S. Virtanen, High temperature oxidation of γ/γ' strengthened Co-base superalloys, Corros. Sci., 53 (2011) 2027–2034.

[13] J. R. Davis, editor, Heat resistant materials, ASM Intl., first ed., Ohio, 1997.

[14] H. Y. Yan, V. A. Vorontsov, and D. Dye, Alloying effects in polycrystalline γ' strengthened Co-Al-W base alloys, Intermet., (2013), http://dx.doi.org/10.1016/j.intermet.2013.10.022 (corrected proof online).

[15] N.B. Pilling and R. E. Bedworth, The oxidation of metals at high temperatures, J. Inst. Met., 29 (1923) 529–591.

[16] M. G. Hebsur and R. V. Miner, High temperature isothermal and cyclic oxidation behavior of a single crystal Ni base superalloy, J. Mater. Energy Syst., 8 (1987) 363–370.

[17] J. H. DeVan, Catastrophic oxidation of high temperature alloys, Oak Ridge National Laboratory, Report (1961) 1–27.

[18] D. Brandon and W. D. Kaplan, Microstructural Characterization of Materials, John Wiley & Sons, second ed. England, 2008.

[19] J. Goldstein, D. E. Newbury, D. C. Joy, C. E. Lyman, P. Echlin, E. Lifshin, L. Sawyer, and J. R. Michael, Scanning Electron Microscopy and X-ray Microanalysis, Springer, third ed., New York, 2003.

[20] R. Kannan and M. S. Seehra, Percolation effects and magnetic properties of the randomly diluted fcc system $Co_pMg_{1-p}O$, Phys. Rev. B: Condens. Matter, 35 (1987) 6847–6853.

[21] G. Brauer editor, Handbook of Preparative Inorganic Chemistry, volume 1. Academic Press, second ed., New York, 1963.

[22] X. Liu and C. T. Prewitt, High-temperature x-ray diffraction study of Co_3O_4: Transition from normal to disordered spinel, Phys. Chem. Miner., 17 (1990) 168–172.

[23] S. C. Petitto, E. M. Marsh, G. A. Carson, and M. A. Langel, Cobalt oxide surface chemistry: The interaction of CoO(100), Co_3O_4(110), and Co_3O_4(111) with oxygen and water, J. Mol. Catal. A: Chem., 281 (2008) 49–58.

[24] Y. W. D. Chen and R. N. Noufi, Electrodeposition of nickel and cobalt oxides onto platinum and graphite electrodes for alkaline water electrolysis, J. Electrochem. Soc., 131 (1984) 731–735.

[25] M. M. Elsemongy, M. M. A. Gouda, and Y. A. Elewady, New baths for the deposition of manganese and cobalt oxides, J. Electroanal. Chem. Interfacial Electrochem., 76 (1977) 367–373.

[26] L. Lutterotti and P. Scardi, Simultaneous structure and size-strain refinement by the Rietveld method, J. Appl. Cryst., 23 (1990) 246–252.

[27] E. G. Gontier-Moya, G. Erdélyi, F Moya and K. Freitag, Sol-

ubility and diffusion of cobalt in alumina, Philos. Mag. A, 81 (2001) 2665–2673.
[28] H. St. C. O'Neill, Temperature dependence of the cation distribution in $CoAl_2O_4$ spinel, Eur. J. Miner., 6 (1994) 603–609.
[29] W. H. Baur and A. A. Khan, Rutile-type compounds. IV. SiO_2, GeO_2 and a comparison with other rutile-type structures, Acta Cryst., B27 (1971) 2133–2139.
[30] R. E. Newnham and Y. M. de Haan, Refinement of the α Al_2O_3, Ti_2O_3, V_2O_3 and Cr_2O_3 structures, Zeit. Krist., 117 (1962) 235–237.
[31] J. L. Smialek, A deterministic interfacial cyclic oxidation spalling model, Acta Mater., 51 (2003) 469–483.
[32] D. J. Young, High temperature oxidation and corrosion of metals, Elsevier Science, first ed., Oxford, 2008.
[33] P. H. Bolt, F.H.P.M. Habraken, and J. W. Geus, Formation of nickel, cobalt, copper, and Iron aluminates from α- and γ-alumina-supported oxides: a comparative study J. Solid State Chem., 135 (1998) 59–69.
[34] B. Kubota, Decomposition of higher oxides of chromium under various pressures of oxygen, J. Am. Ceram. Soc., 44 (1961) 239–248.
[35] M. H. Li, X. F. Sun, J. G. Li, Z. Y. Zhang, T. Jin, H. R. Guan, and Z. Q. Hu, Oxidation behavior of a single-crystal Ni-base superalloy in air. I: At 800 and 900 °C, Oxid. Met., 59 (2003) 591–605.